NUCLEAR THEORY, Vol. 42 (2025)
eds. M. Gaidarov, N. Minkov, Heron Press, Sofia

Nuclear Constraints and Multimessenger Signatures: Probing the Equation of State of Neutron-Rich Matter

P.S. Koliogiannis[1,2], **E. Yüksel**[3], **T. Ghosh**[1], **N. Paar**[1]

[1]Department of Physics, Faculty of Science, University of Zagreb, Bijenička cesta 32, 10000 Zagreb, Croatia

[2]Department of Theoretical Physics, Aristotle University of Thessaloniki, 54124 Thessaloniki, Greece

[3]School of Mathematics and Physics, University of Surrey, Guildford, Surrey, GU2 7XH, United Kingdom

Abstract. The density dependence of the nuclear symmetry energy is a key ingredient in determining the equation of state of neutron-rich matter, with significant implications for both finite nuclei and neutron stars. Recent experimental advances – including parity violating electron scattering on $^{48}\mathrm{Ca}$ (CREX) and $^{208}\mathrm{Pb}$ (PREX-2), as well as measurements of electric dipole polarizability – provide valuable constraints on isovector nuclear properties. In this work, a class of relativistic energy density functionals is employed to quantify correlations between nuclear observables – such as neutron skin thickness and weak charge form factors – and macroscopic neutron star properties, including radius and tidal deformability. These theoretical correlations are compared with data from both terrestrial experiments and multi-messenger observations of the binary neutron star merger GW170817, yielding constraints on the symmetry energy and the equation of state at supranuclear densities. The results demonstrate that finite-nucleus measurements play important role in constraining the equation of state, particularly when higher-order terms in the symmetry energy expansion are included. Persistent discrepancies among constraints from different nuclear probes highlight the need for more precise measurements and additional astrophysical input to advance our understanding of dense matter.

1 Introduction

A fundamental aspect in physics of neutron stars is the equation of state (EoS) of nuclear matter, as it governs the relation between energy density and pressure and, consequently, the stellar structure. However, the density dependence of the nuclear symmetry energy, particularly at supranuclear densities, remains poorly constrained. These uncertainties propagate directly into the EoS and, in turn, to predictions of neutron star properties. The role of the nuclear symmetry energy is twofold: on the one hand, it enters the isovector channel of the nuclear interaction, influencing the properties of finite nuclei; on the other hand, it constitutes

a key ingredient of the EoS of neutron star matter, affecting stellar structure and macroscopic observables. In this respect, the nuclear symmetry energy serves as an interdisciplinary quantity, bridging terrestrial experiments on finite nuclei with astrophysical observations of neutron stars, and thereby linking nuclear physics with nuclear astrophysics [1–3].

The behavior of the nuclear symmetry energy around saturation density, including its slope parameter, and its correlations with nuclear observables such as weak form factors and neutron skin thickness, have been the subject of extensive studies [4–8]. Closely connected to the density dependence of the symmetry energy are recent parity-violating electron scattering experiments, CREX (^{48}Ca) [9] and PREX-2 (^{208}Pb) [10], which provide direct information on weak form factors and neutron skin thickness. Complementarily, astrophysical observations probe the symmetry energy at higher densities, as it governs neutron star composition, cooling mechanisms, crust structure, and radii [3]. In particular, binary neutron star mergers, such as GW170817 [11], constrain the low-density regime of the EoS through tidal deformability measurements and corresponding limits on the stellar radius. Recent works [12–17] have sought to combine these complementary approaches in order to constrain the density dependence of the symmetry energy and assess its impact on neutron star properties.

In this work, we employ a set of β-equilibrated EoSs for neutron star matter derived from relativistic energy density functionals (EDFs) with density-dependent point-coupling (DD-PC) interactions [17], along with additional EoSs constructed to be consistent with the CREX and PREX-2 results [18]. By using EDFs, which provide a unified description of finite nuclei and neutron stars, we aim to establish direct connections between experimental probes of nuclear matter, i.e., weak form factors and neutron skin thickness, and astrophysical observables such as the radius and tidal deformability of a $1.4\ \mathrm{M}_\odot$ neutron star. In doing so, we place new constraints on the dense-matter EoS. A detailed account of this study has been published in Ref. [19], and the present contribution provides an overview of the main results and their implications for nuclear and astrophysical constraints.

The paper is organized as follows. In Section 2, we present the theoretical framework and EoS models. Results and discussion are given in Section 3, while Section 4 provides the concluding remarks.

2 Framework and Models

In this study, a family of eight DD-PC functionals (DD-PC-J29…36) [17], constructed within the relativistic EDF framework and optimized to ground-state nuclear properties while systematically varying the symmetry energy at saturation ($J = 29$–36 MeV), was employed (for a detailed description see Ref. [19] and references therein). In addition, the functionals DD-PC-CREX, DD-PC-PREX, DD-PC-REX, and DD-PCX [20] were considered, the first three being constrained by weak form factor measurements from CREX and PREX-2, and

the latter by both isovector dipole and isoscalar monopole excitation properties of ^{208}Pb alongside with the nuclear ground-state data. This set of functionals allowed for a broad exploration of nuclear matter properties under varying symmetry energy assumptions.

Building upon these microscopic descriptions of nuclear interactions, the framework was extended to astrophysical scales in order to model neutron stars. In this context, neutron star matter was treated as charge-neutral, β-equilibrated $npe\mu$ matter, with the baryonic energy density and pressure calculated as

$$\mathcal{E}_b(\rho,\delta) = \rho E_b(\rho,\delta), \quad P_b(\rho,\delta) = \rho^2 \frac{\partial E_b(\rho,\delta)}{\partial \rho}. \tag{1}$$

In Eq. (1), $E_b(\rho,\delta)$ is the energy per baryon, defined as

$$E_b(\rho,\delta) = E_b(\rho,0) + \sum_{k=2,4} \delta^k S_k(\rho), \tag{2}$$

where

$$S_k(\rho) = \frac{1}{k!} \frac{\partial^k E_b(\rho,\delta)}{\partial \delta^k}\Big|_{\delta=0}, \tag{3}$$

with $E_b(\rho,0)$ being the energy per baryon of symmetric nuclear matter and $\delta = (\rho_n - \rho_p)/(\rho_n + \rho_p)$ denoting the isospin asymmetry. Within this framework, and including leptonic contributions modeled as a relativistic Fermi gas, the following β-equilibrated EoSs were obtained: (a) a family of EoSs for which the symmetry energy was systematically varied in the range $J = 29$–36 MeV, (b) two EoSs calibrated to the CREX and PREX-2 measurements, respectively, (c) one EoS constrained by the combination of CREX and PREX-2 experiments, and (d) one EoS constrained by dipole polarizability data.

The structure of neutron stars is determined by solving the Tolman–Oppenheimer–Volkoff equations,

$$\frac{dP(r)}{dr} = -\frac{G\mathcal{E}(r)M(r)}{c^2 r^2}\left(1+\frac{P(r)}{\mathcal{E}(r)}\right)\left(1+\frac{4\pi P(r) r^3}{M(r)c^2}\right) \times \left(1-\frac{2GM(r)}{c^2 r}\right)^{-1}, \tag{4}$$

$$\frac{dM(r)}{dr} = \frac{4\pi r^2}{c^2}\mathcal{E}(r), \tag{5}$$

which are solved self-consistently with the EoS of the fluid interior, providing the pressure and enclosed mass profiles as functions of the radial coordinate r, and thus the fundamental properties of neutron stars.

Complementarily, gravitational-wave detections provided insights into the low-density behavior of the EoS through the effective tidal deformability $\tilde{\Lambda}$ for a binary system, defined as

$$\tilde{\Lambda} = \frac{16}{13}\frac{(12q+1)\Lambda_1 + (12+q)q^4\Lambda_2}{(1+q)^5}, \tag{6}$$

where $q = m_2/m_1 \leq 1$ is the binary mass ratio, and Λ_i is the dimensionless tidal deformability of the i-th star. The latter is expressed as [11]

$$\Lambda_i = \frac{2}{3} k_2 \left(\frac{R_i c^2}{M_i G} \right)^5 \equiv \frac{2}{3} k_2 \beta_i^{-5}, \quad i = 1, 2, \tag{7}$$

with k_2 the tidal Love number, $\beta = GM/(Rc^2)$ the stellar compactness, and M_i and R_i the mass and radius of each binary component. Since tidal deformability is highly sensitive to the stellar radius, it establishes a direct link between nuclear interactions and astrophysical observables.

For the crust, the following parameterizations were adopted: the Baym–Pethick–Sutherland [21] EoS for the outer crust, the Feynman–Metropolis–Teller [22] EoS at even lower densities, and the SLy [23] EoS for the inner crust, up to the crust-core transition density $\rho_{\rm tr}$ [23]. The transition density is determined using the thermodynamical method [24], ensuring consistent crust-core matching.

3 Results and Discussion

Neutron star structure is illustrated in Figure 1(a) through the mass-radius relation for the DD-PC EoSs, alongside with astrophysical constraints from pulsar observations, including maximum masses, radius measurements, and the binary

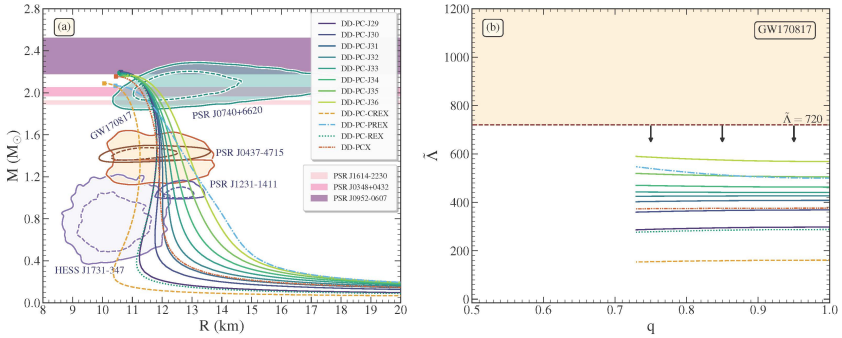

Figure 1. (a) Gravitational mass as a function of the radius for the DD-PC EoSs. The solid lines denote the family of DD-PC EoSs spanning $J = 29, 30, ..., 36$ MeV, while the dashed, dash-dotted, dotted, and dash-dot-dotted lines correspond to the DD-PC-CREX, DD-PC-PREX, DD-PC-REX, and DD-PCX EoSs, respectively. The shaded contours from bottom to top represent the HESS J1731-347 remnant [25], the PSR J1231-1411 [26], the PSR J0437-4715 [27], the GW170817 event [11], and the PSR J0740+6620 [28, 29], while the horizontal shaded regions denote the PSR J1614-2230 [30], PSR J0348+0432 [31], and PSR J0952-0607 [32] pulsar observations with possible maximum neutron star mass. (b) The corresponding effective tidal deformability as a function of the binary mass ratio. The shaded region represents the excluded values provided by LIGO for the GW170817 event [11].

merger GW170817 [11,25–32]. All EoSs satisfied the maximum mass and mass-radius limits, with the lower-J models ($J = 29$–32 MeV) additionally consistent with the ultra-light compact object HESS J1731-347 [25]. Additionally, Figure 1(b) displays the effective tidal deformability as a function of the binary mass ratio, confirming that all EoSs remained within the GW170817 constraints.

Subsequently, attention was directed toward the correlations between nuclear and astrophysical observables. Figure 2 displays the dimensionless tidal deformability $\Lambda_{1.4}$ at $1.4\,\mathrm{M}_\odot$ as a function of the charge-weak form factor difference $F_{\rm ch} - F_{\rm w}$ and the neutron skin thickness $R_{\rm np}$ for ^{48}Ca and ^{208}Pb. It is noted that in both cases, the observables exhibit an exponential dependence, where the DD-PC family of EoSs follows closely, while larger deviations are observed for the remaining models, particularly DD-PC-CREX and DD-PC-PREX.

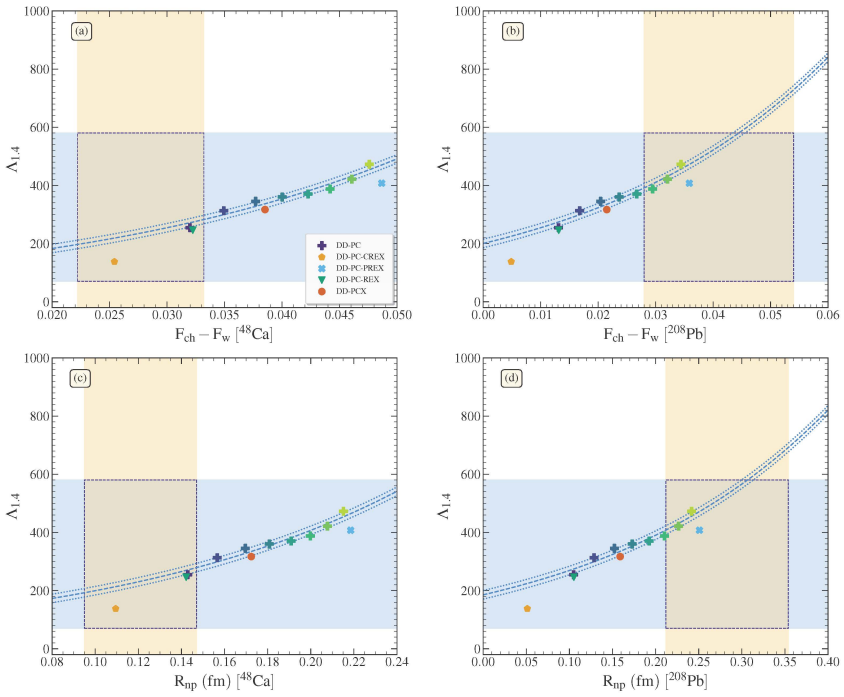

Figure 2. Dimensionless tidal deformability at $1.4\,\mathrm{M}_\odot$ as a function of (a,b) the difference between charge and weak form factors and (c,d) the neutron skin thickness for ^{48}Ca (left panel) and ^{208}Pb (right panel) nuclei. The horizontal shaded region represents the constraints from GW170817 event [11], while the vertical shaded regions correspond to the experimental constraints extracted from (a,c) CREX and (b,d) PREX-2. The symbols denote different EoSs: DD-PC family of EoSs (plus signs, where lighter color denotes higher values of J), DD-PC-CREX (pentagon), DD-PC-PREX (cross), DD-PC-REX (triangle), and DD-PCX (circle). The dashed line represents the fit corresponding to the DD-PC family of EoSs, while the dotted lines denote the standard deviation.

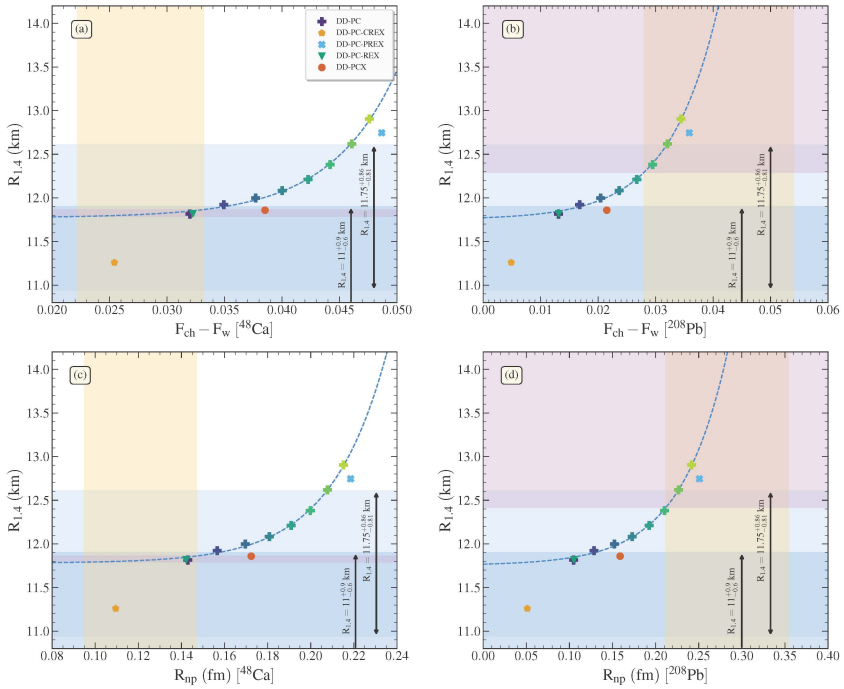

Figure 3. Radius at 1.4 $M_\odot$ as a function of (a,b) the difference between charge and weak form factors and (c,d) neutron skin thickness for the ^{48}Ca (left panel) and ^{208}Pb (right panel) nuclei. The vertical shaded region represents the experimental constraints extracted from (a,c) CREX and (b,d) PREX-2, while the horizontal shaded regions correspond to constraints extracted from Refs. [33, 34]. The symbols denote different EoSs: DD-PC family of EoSs (plus signs, where lighter color denotes higher values of J), DD-PC-CREX (pentagon), DD-PC-PREX (cross), DD-PC-REX (triangle), and DD-PCX (circle). The dashed line represents the fit corresponding to the DD-PC family of EoSs (since $\sigma \ll 0.1$, the standard deviation is not plotted).

Figure 2 also displays constraints on nuclear and astrophysical observables as vertical and horizontal bands, respectively. Their intersections define specific regions of EoSs consistent with both charge-weak form factor and neutron skin thickness. This agreement is expected, since these nuclear observables are strongly correlated. From the astrophysical perspective, all EoSs remain compatible with GW170817. However, from the nuclear physics side, CREX favors models with the lowest symmetry energy, while PREX-2 favors those with $J \gtrsim 35$ MeV. This tension is directly reflected in the CREX- and PREX-2 constrained functionals (DD-PC-CREX and DD-PC-PREX). The same dependence is further illustrated in Figure 3, which shows the neutron star radius $R_{1.4}$ at 1.4 $M_\odot$ as a function of $F_{\rm ch} - F_{\rm w}$ and $R_{\rm np}$ for ^{48}Ca and ^{208}Pb. The above

Table 1. Coefficients of expression (8) for ^{48}Ca and ^{208}Pb nuclei for $\mathcal{Q} = \Lambda_{1.4},\ R_{1.4}$, and $\mathcal{N} = F_{\rm ch} - F_{\rm w},\ R_{\rm np}$. In addition, the standard deviation, σ, and the coefficient of determination, R^2, are also noted. The units of coefficients and σ are defined so $\Lambda_{1.4}$ and $F_{\rm ch} - F_{\rm w}$ to be dimensionless, $R_{1.4}$ to be in km, and $R_{\rm np}$ to be in fm.

	Nuclei	$\mathcal{N}$	c_1	c_2	c_3	σ	R^2
$\Lambda_{1.4}$	^{48}Ca	$\mathrm{F_{ch} - F_w}$	94.946	32.874	–	14.611	0.944
		$\mathrm{R_{np}}$	97.846	7.129	–	14.674	0.944
	^{208}Pb	$\mathrm{F_{ch} - F_w}$	200.443	23.895	–	14.768	0.943
		$\mathrm{R_{np}}$	185.554	3.719	–	14.751	0.943
$\mathrm{R_{1.4}}$	^{48}Ca	$\mathrm{F_{ch} - F_w}$	3.084×10^{-4}	172.174	11.772	0.019	0.997
		$\mathrm{R_{np}}$	2.931×10^{-4}	38.317	11.779	0.019	0.997
	^{208}Pb	$\mathrm{F_{ch} - F_w}$	2.068×10^{-2}	116.622	11.752	0.018	0.997
		$\mathrm{R_{np}}$	1.374×10^{-2}	18.282	11.754	0.018	0.997

correlations are quantified by the exponential expression

$$\mathcal{Q} = c_1 \exp(c_2 \mathcal{N}) + c_3\,, \tag{8}$$

with $\mathcal{Q} = \Lambda_{1.4}, R_{1.4}$ and $\mathcal{N} = F_{\rm ch} - F_{\rm w}, R_{\rm np}$. The fitted coefficients, standard deviations, and R^2 values are summarized in Table 1. These relationships allow CREX and PREX-2 measurements to be mapped onto neutron star radii and symmetry energy constraints: (a) CREX favors $R_{1.4} \in [11.790, 11.861]$ km and $J \in [24.306, 29.037]$ MeV, while (b) PREX-2 favors $R_{1.4} \geq 12.417$ km and $J \geq 34.190$ MeV, revealing a gap of about 0.5 km between the two predictions [19].

Since the radius is intrinsically connected to the tidal deformability, we also employ the relation $\Lambda_{1.4} = c_4 R_{1.4}^{c_5}$, with $c_4 = 5.389 \times 10^{-4}$ and $c_5 = 5.357$ (correlation coefficient: $r = 0.957$, $R^2 = 0.897$), to provide a general behavior of the DD-PC EoSs, as shown in Figure 4. By imposing the observational upper limit on $\Lambda_{1.4}$ from GW170817, the stellar radius is restricted to $R_{1.4} \leq 13.366$ km, consistent with earlier findings. Interestingly, this value lies within the region suggested by PREX-2, and thus can be translated into an upper limit for the symmetry energy at saturation, $J \leq 36.658$ MeV. While CREX and PREX-2 offer uncertainties of comparable magnitude, their implications differ: CREX favors lower J values, yielding a relatively narrow radius band associated with the flatter part of the exponential relation, whereas PREX-2 favors higher J values, leading to a broader radius range connected with the steeper part of the curve.

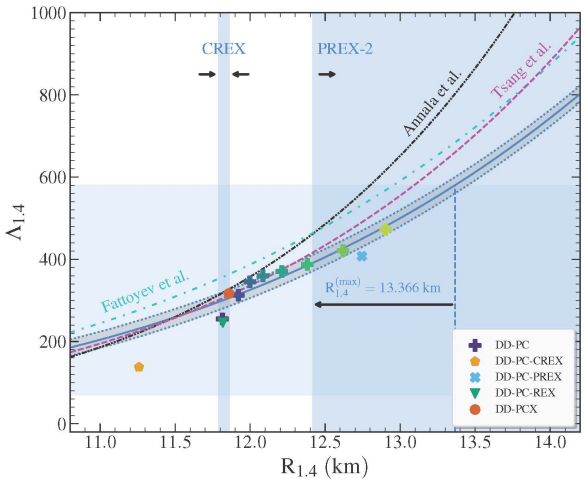

Figure 4. Dimensionless tidal deformability as a function of the radius at 1.4 $M_\odot$ for the DD-PC EoSs. The horizontal shaded region represents the GW170817 event [11], while the vertical shaded regions correspond to the constraints derived in this work [19]. The blue solid line represents the fit for the DD-PC family of EoSs, with the dotted lines denoting the standard deviation. Additional comparisons include expressions from Refs. [35–37].

4 Conclusion

In this work, we have explored the connection between nuclear and neutron star observables within the framework of relativistic EDFs. By employing a set of EoSs based on relativistic DD-PC interactions, including variants consistent with CREX and PREX-2 experiments, we have investigated how weak form factors and neutron skin thickness measurements can be translated into constraints on nuclear symmetry energy, neutron star radii, and tidal deformabilities. The analysis confirms consistency of the DD-PC EoSs with previous investigations and highlights the contrasting implications of CREX and PREX-2: CREX indicates a softer EoS at saturation, while PREX-2 points toward a stiffer EoS. Using the established relationships between finite-nucleus and neutron star properties, constraints on $R_{1.4}$ and J were derived. Remarkably, the DD-PC-REX EoS follows the general behavior of the DD-PC family, yielding well-defined values for $R_{1.4}$ and J within the CREX-allowed region.

Future improvements in both experimental precision and astrophysical measurements, particularly from next-generation gravitational-wave detectors and parity-violating electron scattering experiments, are expected to further narrow the allowed EoSs. Such advances will provide a more unified and quantitative description of dense matter, bridging nuclear physics and neutron star astrophysics.

Acknowledgments

This work is supported by the Croatian Science Foundation under the project number HRZZ-MOBDOL-12-2023-6026 and under the project Relativistic Nuclear Many-Body Theory in the Multimessenger Observation Era (HRZZ-IP-2022-10-7773). This work was supported by the project "Implementation of cutting-edge research and its application as part of the Scientific Center of Excellence for Quantum and Complex Systems, and Representations of Lie Algebras", Grant No. PK.1.1.10.0004, co-financed by the European Union through the European Regional Development Fund - Competitiveness and Cohesion Programme 2021-2027. E.Y. acknowledges support from the UK STFC under award no. ST/Y000358/1.

References

[1] A. Steiner, M. Prakash, J. Lattimer, P. Ellis, *Phys. Rep.* **411**(6) (2005) 325-375.
[2] G.F. Burgio, I. Vidaña, *Universe* **6**(8) (2020) 119.
[3] J.M. Lattimer, *Particles* **6**(1) (2023) 30-56.
[4] X. Roca-Maza, N. Paar, *Prog. Part. Nucl. Phys.* **101** (2018) 96-176.
[5] C. Mondal, B. K. Agrawal, M. Centelles, G. Colò, X. Roca-Maza, N. Paar, X. Viñas, S.K. Singh, S.K. Patra, *Phys. Rev. C* **93** (2016) 064303.
[6] X. Roca-Maza, M. Brenna, G. Colò, M. Centelles, X. Viñas, B.K. Agrawal, N. Paar, D. Vretenar, J. Piekarewicz, *Phys. Rev. C* **88** (2013) 024316.
[7] X. Roca-Maza, X. Vias, M. Centelles, B.K. Agrawal, G. Colò, N. Paar, J. Piekarewicz, D. Vretenar, *Phys. Rev. C* **92** (2015) 064304.
[8] P.-G. Reinhard, J. Piekarewicz, W. Nazarewicz, B.K. Agrawal, N. Paar, X. Roca-Maza, *Phys. Rev. C* **88** (2013) 034325.
[9] D. Adhikari, et al., *Phys. Rev. Lett.* **129** (2022) 042501.
[10] D. Adhikari, et al., *Phys. Rev. Lett.* **126** (2021) 172502.
[11] B.P. Abbott, et al., *Phys. Rev. X* **9** (2019) 011001.
[12] T.-G. Yue, L.-W. Chen, Z. Zhang, Y. Zhou, *Phys. Rev. Res.* **4** (2022) L022054.
[13] R. Essick, I. Tews, P. Landry, A. Schwenk, *Phys. Rev. Lett.* **127** (2021) 192701.
[14] R. Essick, P. Landry, A. Schwenk, I. Tews, *Phys. Rev. C* **104** (2021) 065804.
[15] B.T. Reed, F.J. Fattoyev, C.J. Horowitz, J. Piekarewicz, *Phys. Rev. Lett.* **126** (2021) 172503.
[16] B. Biswas, *Astrophys. J.* **921**(1) (2021) 63.
[17] E. Yüksel, T. Oishi, N. Paar, *Universe* **7**(3) (2021) 71.
[18] E. Yüksel, N. Paar, *Phys. Lett. B* **836** (2023) 137622.
[19] P. Koliogiannis, E. Yüksel, N. Paar, *Phys. Lett. B* **862** (2025) 139362.
[20] E. Yüksel, T. Marketin, N. Paar, *Phys. Rev. C* **99** (2019) 034318.
[21] G. Baym, C. Pethick, P. Sutherland, *Astrophys. J.* **170** (1971) 299.
[22] R.P. Feynman, N. Metropolis, E. Teller, *Phys. Rev.* **75** (1949) 1561-1573.
[23] F. Douchin, P. Haensel, *Astron. Astrophys.* **380**(1) (2001) 151-167.
[24] N. Paar, C.C. Moustakidis, T. Marketin, D. Vretenar, G.A. Lalazissis, *Phys. Rev. C* **90** (2014) 011304.

[25] V. Doroshenko, V. Suleimanov, G. Pühlhofer, A. Santangelo, *Nat. Astron.* **6** (2022) 1444-1451.
[26] T. Salmi, et al., *Astrophys. J.* **976**(1) (2024) 58.
[27] D. Choudhury, et al., *Astrophys. J. Lett.* **971**(1) (2024) L20.
[28] E. Fonseca, et al., *Astrophys. J. Lett.* **915**(1) (2021) L12.
[29] A.J. Dittmann, et al., *Astrophys. J.* **974**(2) (2024) 295.
[30] Z. Arzoumanian, et al., *Astrophys. J. Suppl. S.* **235**(2) (2018) 37.
[31] J. Antoniadis, et al., *Science* **340** (6131) (2013) 1233232.
[32] R.W. Romani, D. Kandel, A.V. Filippenko, T.G. Brink, W. Zheng, *Astrophys. J. Lett.* **934**(2) (2022) L17.
[33] C.D. Capano, I. Tews, S.M. Brown, B. Margalit, S. De, S. Kumar, D.A. Brown, B. Krishnan, S. Reddy, *Nat. Astron.* **4** (2020) 625-632.
[34] T. Dietrich, M.W. Coughlin, P.T.H. Pang, M. Bulla, J. Heinzel, L. Issa, I. Tews, S. Antier, *Science* **370** (6523) (2020) 1450-1453.
[35] E. Annala, T. Gorda, A. Kurkela, A. Vuorinen, *Phys. Rev. Lett.* **120** (2018) 172703.
[36] F.J. Fattoyev, J. Piekarewicz, C.J. Horowitz, *Phys. Rev. Lett.* **120** (2018) 172702.
[37] C. Tsang, M. Tsang, P. Danielewicz, F. Fattoyev, W. Lynch, *Phys. Lett. B* **796** (2019) 1-5.